IX. PLASMAS AND CONTROLLED NUCLEAR FUSION

A. Active Plasma Systems*

Academic and Research Staff

Prof. L. D. Smullin
Prof. A. Bers
Prof. G. D. Bernard
Prof. W. D. Getty
Prof. H. A. Haus
Prof. M. A. Lieberman
Prof. J. G. Siambis

Graduate Students

R. R. Bartsch
S. R. J. Brueck
J. A. Davis
F. N. Herba
B. R. Kusse
J. A. Mangano
R. R. Parker
D. M. Perozek
H. M. Schneider
M. G. Smith
R. E. Tremain, Jr.
R. N. Wallace

1. ELECTRON BEAM EXCITATION OF ION OSCILLATIONS IN AN ECRD PLASMA

A thesis, entitled "Ion Oscillations Excited by Electron Beam-Plasma Interaction," was submitted by Michael A. Lieberman to the Department of Electrical Engineering, M.I.T., June 1966, in partial fulfillment of the requirements for the degree of Doctor of Philosophy.

A. Bers

2. BEAM-PLASMA DISCHARGE: SYSTEM D

Operation with "Asco" Valve Gas Injection

The plasma density as a function of time has been simultaneously measured by the TM_{010} cavity-mode shift technique and by 8-mm Fabry-Perot interferometry. The density decay (for the minimum gas pulse necessary for a discharge) is shown in Fig. IX-1. The density has been interpreted from the measurements by assuming that the density profile varies as

$$n(r) = n_e J_o(2.405 r/r_{cavity}). \quad (1)$$

The density decay as measured by the Fabry-Perot interferometer in shown in Fig. IX-2 for several different peak pressures (as measured by the swing of the Veeco gauge).

The x-ray spectrum of the discharge above ~130 keV has been measured during various time intervals to determine the shift of the "temperature" of the hot electrons with time. The normalized spectra are shown in Fig. IX-3.

*This work was supported by the National Science Foundation (Grants GK-57 and GK-1165).

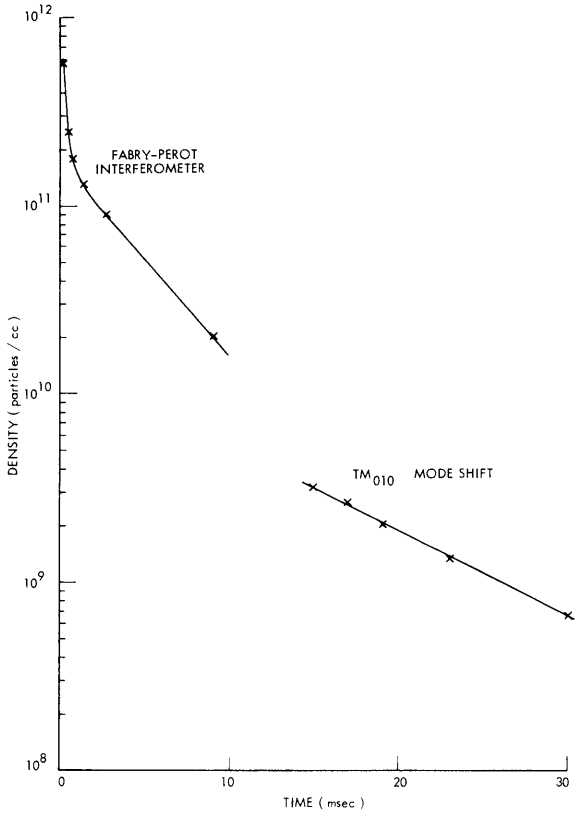

Fig. IX-1.

Density decay for operation with Asco valve.

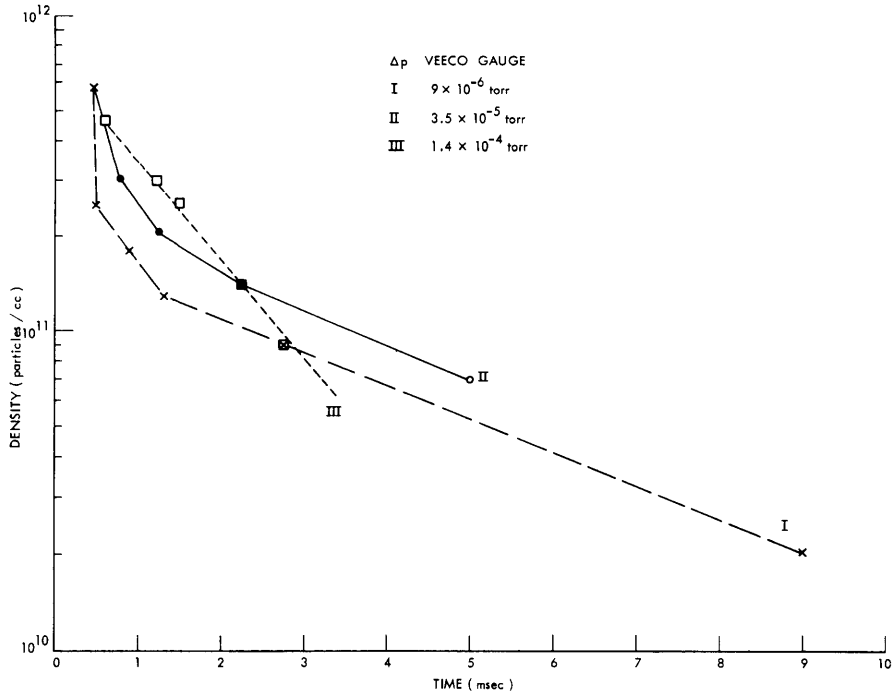

Fig. IX-2. Fabry-Perot interferometer density measurement for operation with Asco valve.

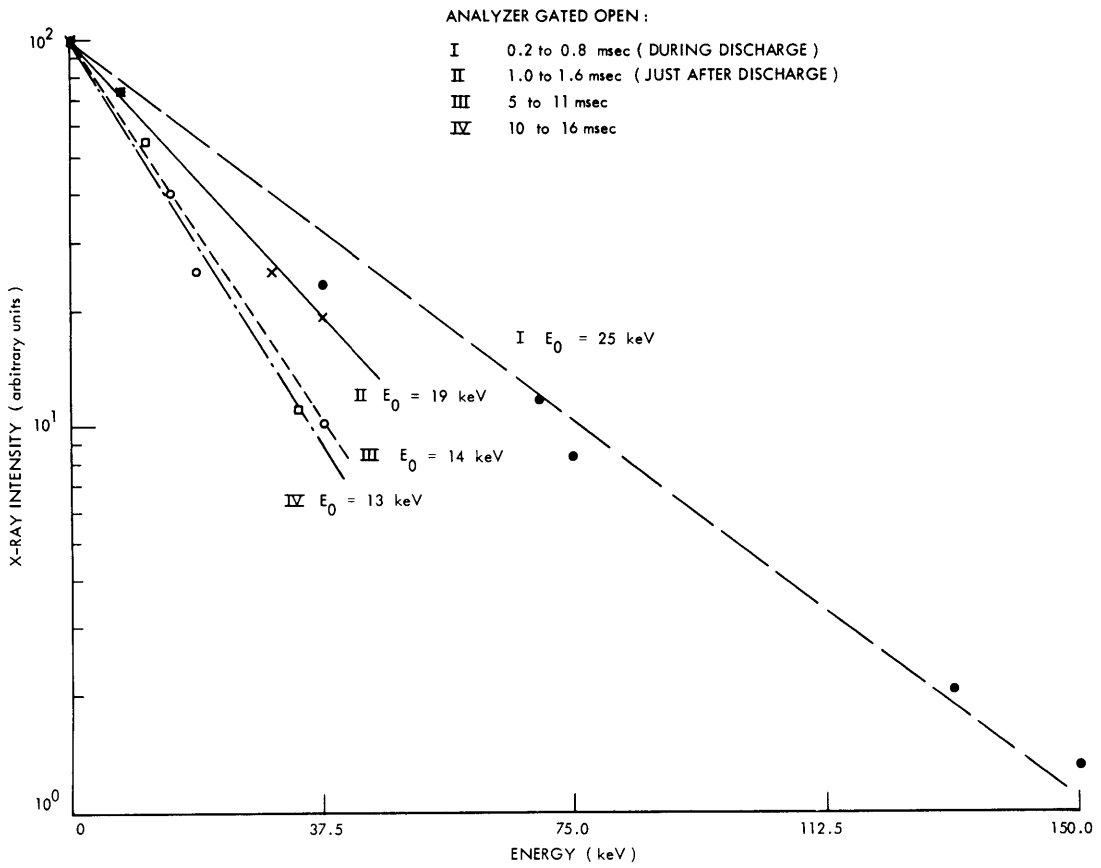

Fig. IX-3. X-ray intensity from discharge.

Operation with Marshall Valve Gas Injection

An electronic drive has been installed on the Marshall valve described previously.[1] The pressure transient as measured by a nude 6AH6 valve is shown in Fig. IX-4. The 6AH6 was located ~2 inches in front of the collector. Similar measurements made for the Asco valve indicate an improvement of ~10 in the rise time of the gas pressure.

Measurements have been made on the discharge obtained with Marshall valve gas injection. The decay following the beam-plasma discharge is observed to be unstable on approximately 50 per cent of the shots.

a. Stable decay: The light output of a stable decay is shown in Fig. IX-5. The peak amplitude of the signal is ~1/10 the peak amplitude of the light signal with Asco valve operation. The uncompensated diamagnetic signal is shown in Fig. IX-6, as an example of the stable decay. The peak amplitude of the diamagnetism is the same ($\sim 10^{14}$ eV/cc) for operation with either valve. The observation that the diamagnetic signal of the stable decay has a hump after the end of the beam pulse was initially interpreted as meaning that the decay time constant of the high-energy electrons was greater than the time constant of flux diffusion. (~20 msec). More complete analysis, by using the method of Parker,[2] gives ~5 msec for the initial decay time constant of the hot-electron density.

The stable density decay has been measured by the techniques used previously on the discharges obtained with the Asco valve. The output of the 4-mm interferometer is shown in Fig. IX-7. Figures IX-8 and IX-9, show the stable density decay for operation with the Marshall valve (interpreted with the plasma radial variation as given by Eq. 1). The light-intensity profile of the discharge was found with the apparatus shown in Fig. IX-10a. The resulting profile corrected for the change of the effective window area with angle is shown in Fig. IX-10b.

b. Unstable decay: The unstable decay is characterized by a sharp drop in the diamagnetic signal. This is accompanied by a sharp drop in the light signal and is illustrated in Fig. IX-11. A burst of x-rays is emitted at the time of the drop of the diamagnetism. This is shown in Fig. IX-12. The spectrum of the emitted radiofrequency has been found to be in the 2-4 kMc range at the time of the instability. The results of suitably filtering the output of a 3/4 inch loop are shown in Fig. IX-13. The X-band output was taken with a waveguide window on the discharge tube. A 2 ft length of S-band waveguide was used as a cutoff filter, and care was always taken to isolate the crystal detector from the system. The observed range of frequencies is in the range of the electron-cyclotron frequency (B_o = 1 to 6 kGauss).

The high-energy x-ray spectrum is shown in Fig. IX-14. The "temperature" is observed to be 51 keV; however, the spectrum analyzer would only detect x-ray energies above ~130 keV. The pulse height analyzer is being repaired and this

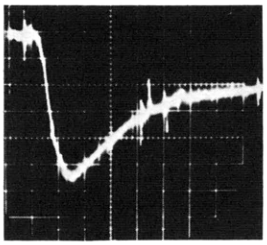

2 msec / cm

Fig. IX-4. Marshall valve pressure transient.

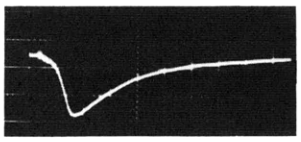

0.5 msec / cm

Fig. IX-5. Marshall valve operation: stable light decay.

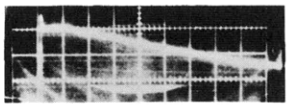

5 msec / cm

Fig. IX-6. Marshall valve operation: stable diamagnetic decay.

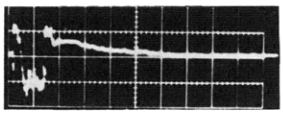

500 μsec / cm

Fig. IX-7. Marshall valve operation: 4-mm interferometer density measurement.

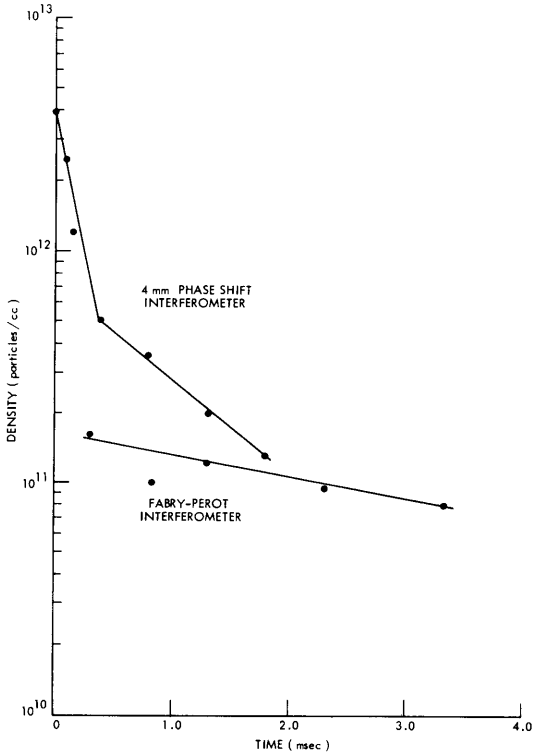

Fig. IX-8. Density decay for Marshall valve operation (high-density range).

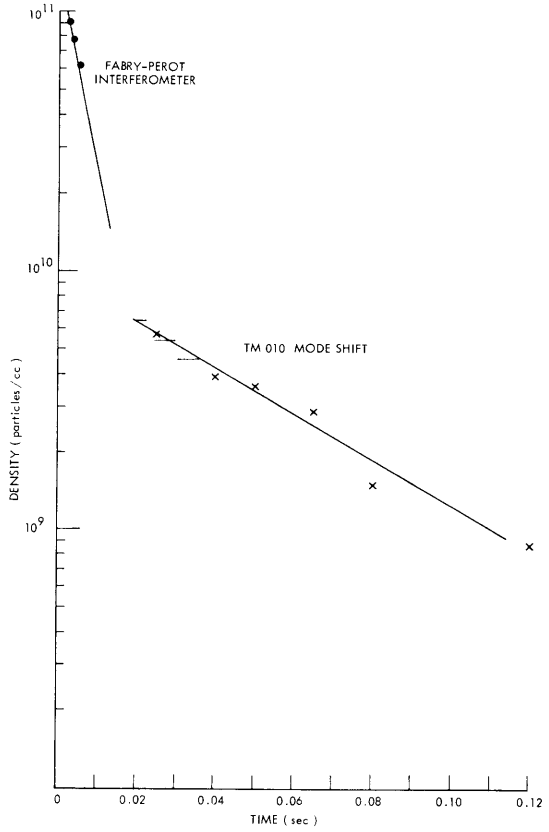

Fig. IX-9. Density decay for Marshall valve operation (low-density range).

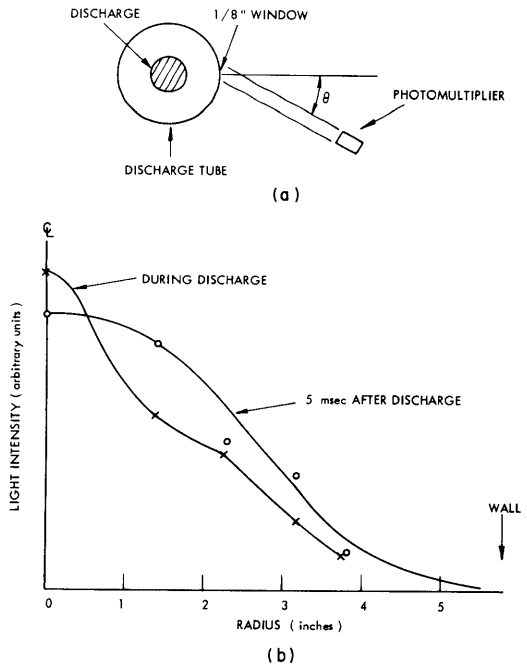

Fig. IX-10. (a) Light-profile apparatus. (b) Light-intensity profile.

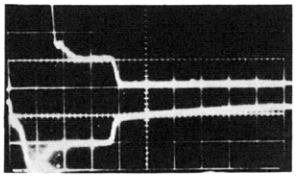

Fig. IX-11. Instability with Marshall valve operation: light and diamagnetism.

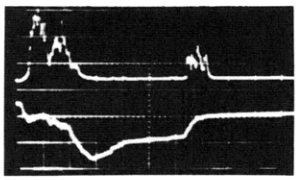

Fig. IX-12. Instability with Marshall valve operation: x-ray and diamagnetism.

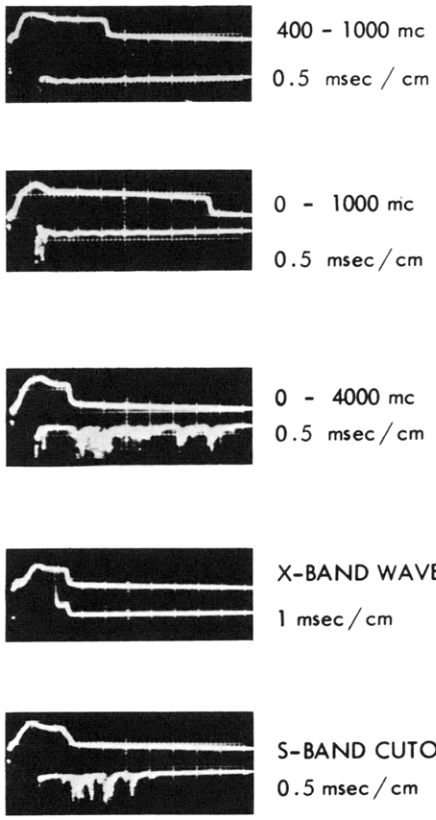

Fig. IX-13. Filtered RF output from discharge.

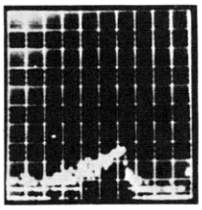

Fig. IX-14. High-energy x-ray spectrum.

measurement will be repeated for a lower energy range (20-60 keV).

Construction of circuits to provide a DC beam of up to 1 kV energy is complete. Experimental investigation of the heating at the ion plasma frequency will be attempted in the afterglow where the plasma consists of hot electrons.[3]

The calibration of the Veeco gauge with a new McLeod gauge is under way at present. Knowledge of the H_2 density will make it possible to compare the decay model described previously with the experimental observations.[4]

The author wishes to acknowledge the use of the facilities of the National Magnet Laboratory for the experiments described here.

R. R. Bartsch

References

1. R. R. Bartsch, Quarterly Progress Report No. 82, Research Laboratory of Electronics, M. I. T., July 15, 1966, pp. 131-137.
2. R. R. Parker, Quarterly Progress Report No. 76, Research Laboratory of Electronics, M. I. T., January 15, 1965, p. 105.
3. M. A. Lieberman, Ph. D. Thesis, Department of Electrical Engineering, M. I. T., June 1966, Chap. IV.
4. R. R. Bartsch, Quarterly Progress Report No. 80, Research Laboratory of Electronics, M. I. T., January 15, 1966, pp. 128-132.

3. HIGH-FREQUENCY ELECTRON-PHONON INTERACTIONS IN A MAGNETIC FIELD

We have previously reported[1] on an analysis of the classical dispersion relation for electrons interacting with acoustic waves in a solid. With parallel applied DC electric and magnetic fields the dispersion relation in the quasi-static approximation ($\bar{q} \parallel \bar{E}$) is

$$K_p + K_e - 1 = 0 \tag{1}$$

$$K_p = \frac{\omega^2 - q^2 s^2}{\omega^2 - q^2 s^2 + Cq^4} \tag{2}$$

$$K_e = 1 + \frac{\omega_p^2}{q^2} \int_{-\infty}^{\infty} dw_{\parallel} \int_0^{\infty} 2\pi w_{\perp} dw_{\perp} \sum_n \frac{J_n^2(p)\left(\frac{n\omega_c}{w_{\perp}} \frac{\partial f_{01}}{\partial w_{\perp}} + q_{\parallel} \frac{\partial f_{01}}{\partial w_{\parallel}}\right)}{(\omega - q_{\parallel} w_{\parallel} - n\omega_c)} \tag{3}$$

Here, s is the sound velocity, ω_p is the electron plasma frequency, ω_c is the electron-cyclotron frequency, $q_{\parallel}$ is the wave-number component along B_0, $q_{\perp}$ is the wave-number component across B_0, $p = q_{\perp} w_{\perp}/\omega_c$, C is the coupling constant and electron-lattice collisions and phonon decay have been ignored. For parameters typical of InSb at 77°K and carrier concentrations $\approx 2 \times 10^{14}/cm^3$, Maxwell-Boltzmann statistics are appropriate,

and hence

$$f_{01} = \frac{1}{(2\pi)^{3/2} v_T^3} \exp\left\{-\left[w_\perp^2+(w_{||}-v_D)^2\right]\Big/2v_T^2\right\}, \tag{4}$$

where v_T is the thermal velocity, and v_D the drift velocity.

Our earlier analysis of the zero magnetic field case was incorrect; the corrected curves of the imaginary part of ω (growth) vs angle of propagation for various electric

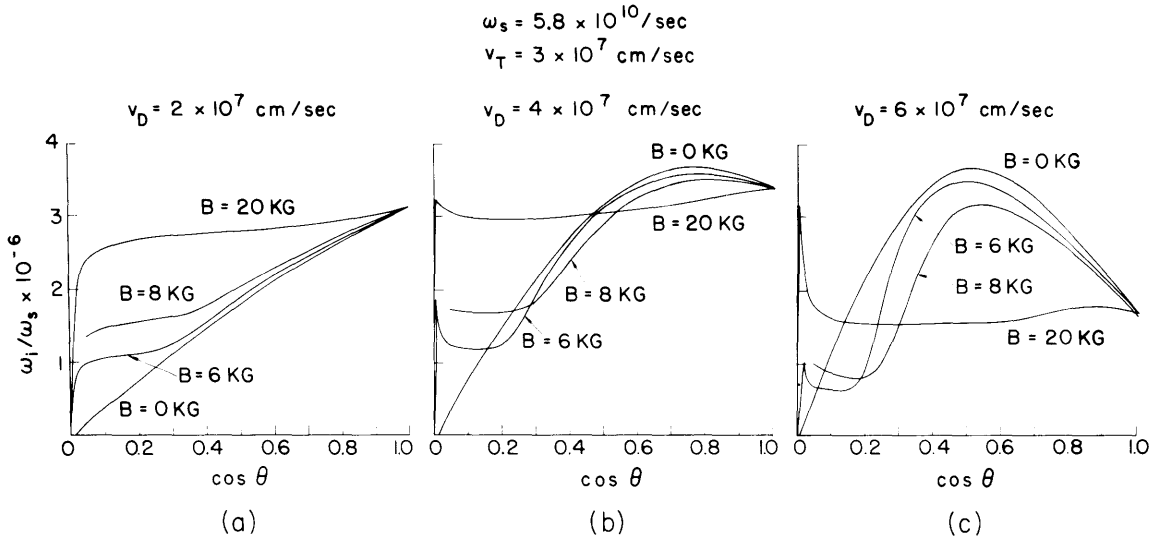

Fig. IX-15. Variation of amplification with direction of propagation. The small cos θ variation has been included only for B = 20 kGauss and B = 6 kGauss.

and magnetic fields appear in Fig. IX-15. As we have previously noted,[1] the growth rate is primarily determined by the imaginary part of the electron dispersion relation.

Zero Magnetic Field

For zero magnetic field the electron dispersion relation reduces to

$$K_e = 1 + \frac{\omega_p^2}{q^2} \int \frac{\bar{q} \cdot (\partial f_{01}/\partial \bar{w})}{(\omega - \bar{q} \cdot \bar{w})} d^3w.$$

The general features of the growth curves in Fig. IX-15 can readily be interpreted on the basis of this equation. The physical mechanism is anti-Landau damping. Figure IX-16 is a plot of the distribution function f_{01} along the direction of propagation. The

anti-Landau damping is expected to be greatest when the electrons near the point of inflection in f_{01} at $w_q = v_D \cos\theta - v_T$ are moving at the wave phase velocity, or

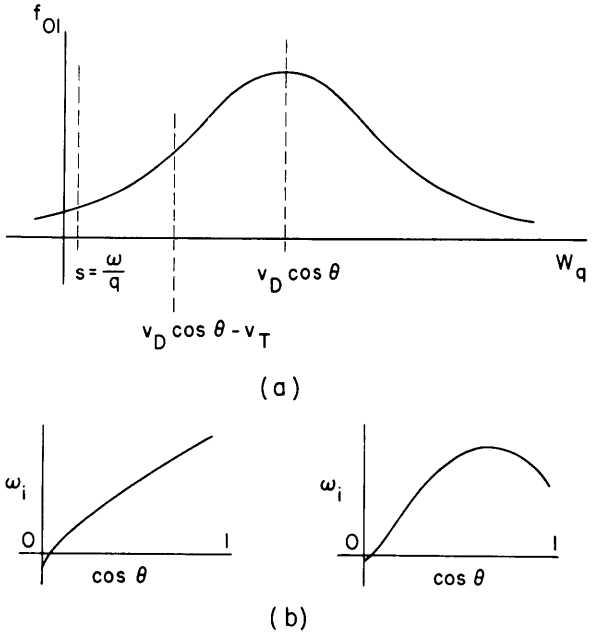

Fig. IX-16. (a) Distribution function f_{01}. (b) Expected variation in growth rate with respect to angle of propagation for $v_D < v_T$ and $v_D > v_T$.

$\cos\theta = (s+v_T)/v_D$. It should be noted that for $s + v_T > v_D$ the peak in the growth rate will occur at $\cos\theta = 1$, that is, for propagation along the electric field.

Finite Magnetic Field

When a magnetic field is added the situation becomes considerably more complicated. A new absorption and growth mechanism arises, because of the possibility of cyclotron resonance, and also the anisotropy introduced by the magnetic field invalidates the Landau-damping argument used above for the component of the wave across the magnetic field.

In order to give a physical interpretation of the growth rates, it is convenient to consider the acoustic wave as being drifted rather than the electrons. The dispersion relation, $\omega^2 = \left(q_\perp^2+q_{||}^2\right)s^2$, of the acoustic wave is shown in Fig. IX-17. The dotted line on this curve represents the drift velocity. Subject to the constraint of a fixed ω and a fixed $\tan\theta = \frac{q_\perp}{q_{||}}$, it can be shown that the wave becomes negative energy for $\cos\theta > \frac{\omega}{qv_D} = \frac{s}{v_D}$, and the electrons can be thought of as providing the resistive medium to drive the instability.

Consider, first, the $\frac{\partial f_{01}}{\partial w_{||}}$ term in Eq. 3. The mechanism represented by this term is associated with variations in velocity along the magnetic field and the Landau-damping

argument given above can be applied, with the added feature that now resonances are possible at all cyclotron harmonics. The Bessel functions, whose argument is the ratio

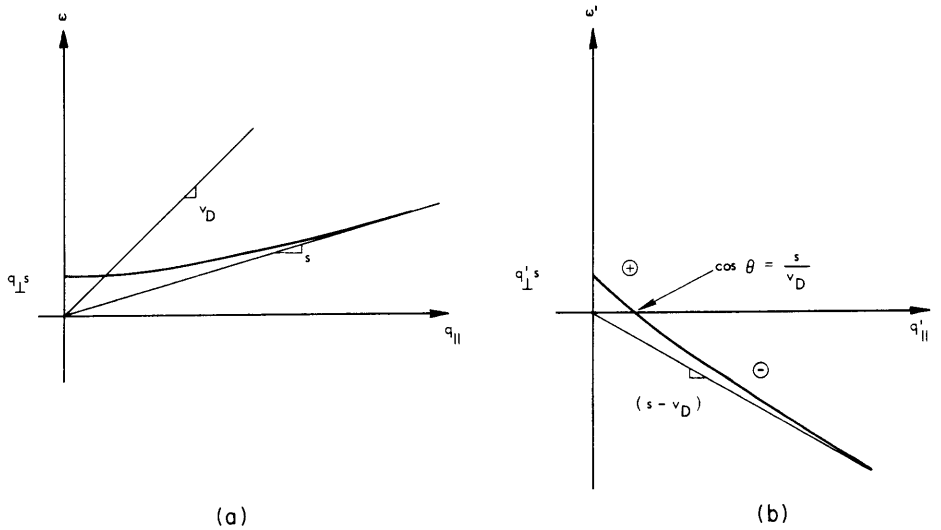

Fig. IX-17. Acoustic-wave dispersion diagram ($q_\perp$ is the parameter). (a) Laboratory frame. (b) Electron frame with velocity v_D.

of 2π times the Larmor radius of the electrons to the wavelength in the perpendicular direction, give a measure of how the electrons move in achieving this resonance. For example, if an electron has a very large $w_\perp$ so that in the course of one cyclotron period it moves across and back, say, 5 or 6 perpendicular wavelengths, then the net affect would be expected to be small.

There is another mechanism which is given by the $\frac{\partial f_{01}}{\partial w_\perp}$ term in Eq. 3. This effect can be explained physically by transforming to a frame moving with the electrons that are in cyclotron resonance with the wave. In this frame, again, with the Bessel function giving some measure of the strength of the interaction, the electrons see a coherent force throughtout their orbit, and hence may either give up energy to the wave or take energy from the wave, their action depending upon their initial phase relationship. As there are more particles with smaller orbits, however, the net effect is to take energy from the wave in this coordinate system.

In order to determine the sign of the interaction in the laboratory frame, it is only necessary to transform the acoustic wave to the moving frame and determine whether or not it is negative energy. For this transformation,

$$\omega^1 = \omega - q_\parallel w_\parallel = \omega - q_\parallel \left(\frac{\omega - n\omega_c}{q_\parallel} \right)$$

or

$$\omega^1 = n\omega_c,$$

so that for all of the resonances at negative n the wave is negative energy. Since the magnitude of the interaction scales as

$$\frac{f_{01}(w_{||})}{q_{||}} \propto \frac{e^{-(w_{||}-v_D)^2/2v_T^2}}{q_{||}}$$

(see Fig. IX-18), the net effect is such as to drive the wave unstable. Again, with

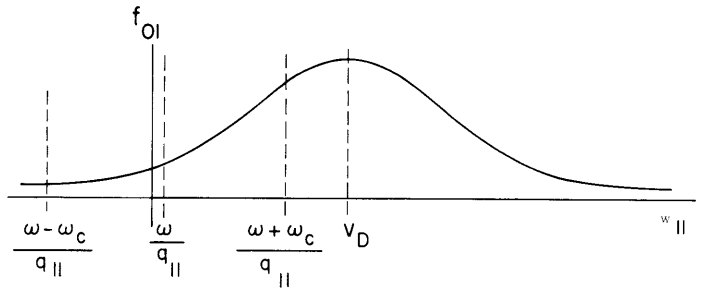

Fig. IX-18. Distribution function along $w_{||}$. For the $n = \pm 1$ terms the wave interacts with the electrons at $w_{||} = \frac{\omega \pm \omega_c}{q_{||}}$. The expected variation in growth rate with $v_D < v_T$ and $v_D > v_T$ is then as shown in Fig. IX-15.

reference to Fig. IX-18, it is evident that the greatest gain will be obtained near $\frac{\omega + \omega_c}{q_{||}} = v_D$, or $\cos\theta = (\omega+\omega_c)/qv_D$. Thus the effect of the magnetic field is to bring electrons with parallel velocities much greater than the phase velocity of the wave into resonance with the wave.

S. R. J. Brueck, A. Bers

References

1. A. Bers and S. R. J. Brueck, "High-Frequency Electron-Phonon Interactions in a Magnetic Field," Quarterly Progress Report No. 81, Research Laboratory of Electronics, M.I.T., April 15, 1966, pp. 106-111.

IX. PLASMAS AND CONTROLLED NUCLEAR FUSION*

B. Applied Plasma Physics Related to Controlled Nuclear Fusion

Academic and Research Staff

Prof. D. J. Rose
Prof. T. H. Dupree
Prof. L. M. Lidsky
Prof. E. P. Gyftopoulos

Graduate Students

R. W. Flynn
R. A. Hill
C. S. Ribbeck
C. E. Wagner
J. C. Woo

1. STUFFED-CUSP PLASMA EXPERIMENT

Construction has been completed on the stuffed-cusp plasma facility. The experimental apparatus has been described previously.[1] The stuffed-cusp magnetic field is generated by a pair of coils operated steady state and a 3-sec pulsed axial current driven by a bank of 12-Volt storage batteries. The required current of 15 KA is obtained by using 11 batteries connected in parallel. Switching is by means of a rack of knife switches driven by a pneumatic cylinder; each battery is switched in parallel to minimize the contact resistance of the circuit breaker. The batteries are then connected in series for recharging.

A pulsed electron beam (1A, 10 kV, 1 msec) is injected through the ring cusp. A beam-plasma discharge is obtained in both cusped and stuffed-cusp geometries in He gas. Diagnostics used thus far have been the monitoring of the RF spectrum with an SP4-A spectrum analyzer, the x-ray output with plastic scintillators, and the light output with a phototube. The results are still preliminary.

Experiments have been proposed to study the effects of the nonzero minimum of the induction on the confinement and stability properties of the cusp.

C. E. Wagner, L. M. Lidsky

References

1. C. E. Wagner and L. M. Lidsky, Stuffed Cusp Plasma Facility, Quarterly Progress Report No. 77, Research Laboratory of Electronics, M.I.T., April 15, 1965.

*This work was supported by the National Science Foundation (Grant GK-1165).